ADVANCED MATERIALS
www.advmat.de

Reprogrammable Mechanical Metamaterials via Passive and Active Magnetic Interactions

Carlos Perez-Garcia, Ramon Zaera, Josue Aranda-Ruiz, Giovanni Bordiga, Giada Risso, Maria Luisa Lopez-Donaire, Katia Bertoldi, and Daniel Garcia-Gonzalez**

This study experimentally demonstrates the reprogrammability of a rotating-squares-based mechanical metamaterial with an embedded array of permanent magnets. How the orientation, residual magnetization, and stiffness of the magnets influence both the static and dynamic responses of the metamaterial is systematically investigated. It is showed that by carefully tuning the magnet orientation within the metamaterial, notable tunability of the metamaterial response can be achieved across static and dynamic regimes. More complex magnetic node configurations can optimize specific structural responses by decoupling the tunability of quasi-static stress–strain behavior from energy absorption under impact loading. Additionally, reprogrammability can be further enhanced by an external magnetic field, which modulates magnetic interactions within the structure. This work paves the way for developing engineered structural components with adaptable mechanical responses, reprogrammable through either the redistribution of magnetic elements or the application of an external magnetic field.

1. Introduction

The pursuit of advanced structural systems endowed with tunable mechanical properties has generated considerable interest in artificially engineered materials designed to exhibit characteristics unattainable in natural materials. In general, the mechanical properties of metamaterials are predominantly influenced by the intricate geometry and spatial tessellation of their cellular microstructures,[1] as opposed to their material composition. In recent years, these metamaterials have garnered significant interest owing to their uncommon mechanical properties, including negative or zero Poisson's ratio,[2–4] negative compressibility,[5,6] as well as other remarkable attributes.[7–10] Further, design efforts have been directed toward achieving tunability in conventional structural properties such as stiffness[11–14] and energy absorption through deformation.[14–16] This is accomplished using complex geometries that permit substantial variations in these properties to meet specific design requirements. Additionally, metamaterials have also enabled the design of reusable structures for impact mitigation[14,15,17–19] – a domain of critical importance across a diverse array of applications.[20] This approach is particularly promising for managing cyclic or recurrent impacts. Nevertheless, in most of the studies, the metamaterials exhibit deformation properties that are fully determined by their undeformed geometry, therefore constraining their range of functionality.

Stimuli-responsive metamaterials have demonstrated the ability to adapt dynamically to changes in their surrounding environments.[21,22] These materials have enabled the realization of architectures capable of changing their properties in response to external stimuli, such as thermal,[23–27] electric,[28,29] chemical,[30,31] electrochemical,[32] pressure,[33,34] magnetic,[35,36] or light actuation.[37,38] Of these, magnetic actuation provides unique advantages, including rapid response, reversible deformations, and untethered functionality in confined spaces. Given these advantages, the impact of magnetic interactions on the response of mechanical metamaterials has been investigated. For instance, it has been shown that permanent magnets embedded within metamaterials can make them multistable[23,39] and tune their mechanical wave transmission.[39,40] Additionally, magnetic interactions offer a promising platform to realize mechanical metamaterials with reprogrammable response. In structures made from magneto-active soft materials, shape reprogrammability has been achieved by heating the thermoplastic matrix above its melting point and then applying a magnetic field during cooling to reorient soft-magnetic particle chains.[41–43] This reprogrammability requires special thermo-magnetic devices and its application is not straightforward, involving heating, magnetization and cooling stages. In structures with embedded

C. Perez-Garcia, R. Zaera, J. Aranda-Ruiz, M. L. Lopez-Donaire, D. Garcia-Gonzalez
Department of Continuum Mechanics and Structural Analysis
Universidad Carlos III de Madrid
Calle Butarque 15, Leganes 28911, Madrid, Spain
E-mail: danigarc@ing.uc3m.es
G. Bordiga, G. Risso, K. Bertoldi
School of Engineering and Applied Sciences
Harvard University
Cambridge, MA 02138, USA
E-mail: bertoldi@seas.harvard.edu

The ORCID identification number(s) for the author(s) of this article can be found under https://doi.org/10.1002/adma.202412353

DOI: 10.1002/adma.202412353

permanent rigid magnets, tuning of mechanical responses has been demonstrated by adjusting the orientation of the permanent magnets.[44] However, while this strategy shows promise, experimentally, only the effects on the static response have been explored, and only out-of-plane magnet orientations have been considered, thereby limiting the design space significantly. In addition, the use of rigid magnets limits these solutions preventing soft bulk response of the metastructures.

Building on these recent advancements, we experimentally demonstrate the reprogrammability of a metamaterial with an embedded array of permanent magnets by leveraging their in-plane polarization. We systematically investigate the effect of the orientation, residual magnetization and stiffness of the permanent magnets both on the static and dynamic response of a metamaterial based on the rotating squares mechanism, which has recently attracted significant interest as it displays effective negative Poisson's ratio.[45–47] By adjusting the mechanical stiffness, residual magnetization, and orientation of the magnets within the metamaterial, we achieve significant tunability in both static and dynamic regimes. Moreover, reprogrammability is further enhanced by applying an external magnetic field, which modulates the magnetic interactions. We envision this study as a pathway to designing engineered structural components with customizable mechanical responses, which can be systematically reprogrammed through either redistribution of magnetic elements or an external magnetic field.

2. Results

2.1. Reprogrammable Magneto-Mechanical Metamaterial Unit Cells

We start by evaluating the magneto-mechanical behavior of single unit cells of the considered metamaterial. Such unit cells are composed of an array of 2 × 2 squares with edge of 20 mm connected at their vertices by thin ligaments of length of 1 mm and width of 1 mm (**Figure 1A**). We fabricate these unit cells via molding alternating layers of two elastomeric materials (Green Zhermack Elite Double 32A with Young's modulus E = 1.92 MPa and Pink Zhermack Elite Double 8 with Young's modulus E = 0.35 MPa, see characterization in *Supporting Information*, Figure S1). To generate magnetic interactions, we place a permanent magnet at the center of each square. We consider three types of magnets: i) rigid commercial Neodimium (Nd) magnets; ii) flexible hard-magnetic magnetorheological elastomers (hMREs) with 50% volume ratio of micron-size Nd particles (F50); iii) flexible hMREs with 30% volume ratio of micron-size Nd particles (F30) (see Experimental Section for details on geometry and manufacturing protocols). As shown in Figure 1D, the flexible magnets have a stiffness comparable to that of the elastomers used to cast the unit cells, whereas the commercial magnets are orders of magnitude stiffer. Further, these magnets have different residual magnetization magnitudes resulting in different effective magnetic interaction forces (Figure 1E – see Experimental Section for details on characterization protocol). It should be noted that there is a direct relationship between the Nd content of the magnets and their stiffness, density, and residual magnetization.

The magnetic interactions within a unit cell can be controlled and reprogrammed by tuning both the residual magnetization and orientation of the magnets in the squares. The magnetic configuration can easily be reprogrammed as many times as needed and determines the responses of the structure. To illustrate this point, we focus on three different configurations of permanent magnets (Figure 1B): (*C*1) where the magnets are oriented to generate repulsive forces between all of them; (*C*2) where the magnets generate both attractive and repulsive forces, with vertically aligned magnets attracting and horizontally aligned magnets repelling; and (*C*3) where the magnets are oriented to generate attractive forces between all of them. When a homogeneous magnetic field of 50 mT is applied vertically using electromagnetic coils, distinctly different configurational changes are observed for each magnet setup (Figure 1C). Specifically, in the case of flexible magnets F50 for configuration *C*1, no change is observed, while for *C*2, all squares rotate uniformly, transforming the central square void into an elongated rhombus, but they return to their original configuration once the external magnetic field is removed. In contrast, for configuration *C*3, applying a magnetic field induces a complex configurational change that results from a balance between active magnetic forces and the elastic mechanical constraints imposed by the hinges (note that the Zeeman effect between the magnets and the externally applied field dominates over the dipole–dipole interactions between magnets). While all the magnets attempt to rotate to align with the applied vertical field, the mechanical constraints of the hinges prevent their full rotation. As a result, the system reaches an equilibrium where two squares collapse and two remain fully open. Notably, once the magnetic field is removed, the unit cell transitions into a fully collapsed state, as the magnetic torques generated by the external field disappear, and the attractive dipole–dipole interactions between the magnets dictate the final state of the unit cell.

Interestingly, the orientation and residual magnetization of the magnets not only dictate the configurational changes in response to external magnetic stimuli but also affect the mechanical behavior under passive conditions, i.e., in the absence of magnetic actuation. To explore the passive behavior of the unit cells, we conducted uniaxial compression tests (see experimental protocol in Experimental Section). When the unit cell without magnets is compressed, buckling of the beam-like ligaments connecting the squares triggers a sudden transformation of the square voids into elongated rhombuses.[19,48] This instability leads to a sharp transition from an initial linear response to a stress plateau (continuous line in Figure 1F,G). Crucially, for the unit cells with magnets, the large rotation of the squares induced by buckling alters the relative positions of the permanent magnets, resulting in evolving magnetic interactions that significantly modulate the force-displacement response (Figure 1H–J). In Figure 1F, we explore how residual magnetization impacts the mechanical behavior of the unit cell. Specifically, we compare the experimentally measured force-displacement curves for the unit cell using both rigid and flexible magnets in configuration *C*1. The results show that the repulsive forces between the magnets increase the force required to initiate buckling, with the buckling force rising as the residual magnetization increases. Moreover, because magnetic interactions vary quadratically with the distance between magnets,[49] in the case of rigid magnets with high residual magnetization, the magnetic contribution to the force becomes dominant over the passive elastic contribution. As a result, in the unit cell with rigid magnets, the post-buckling force increases

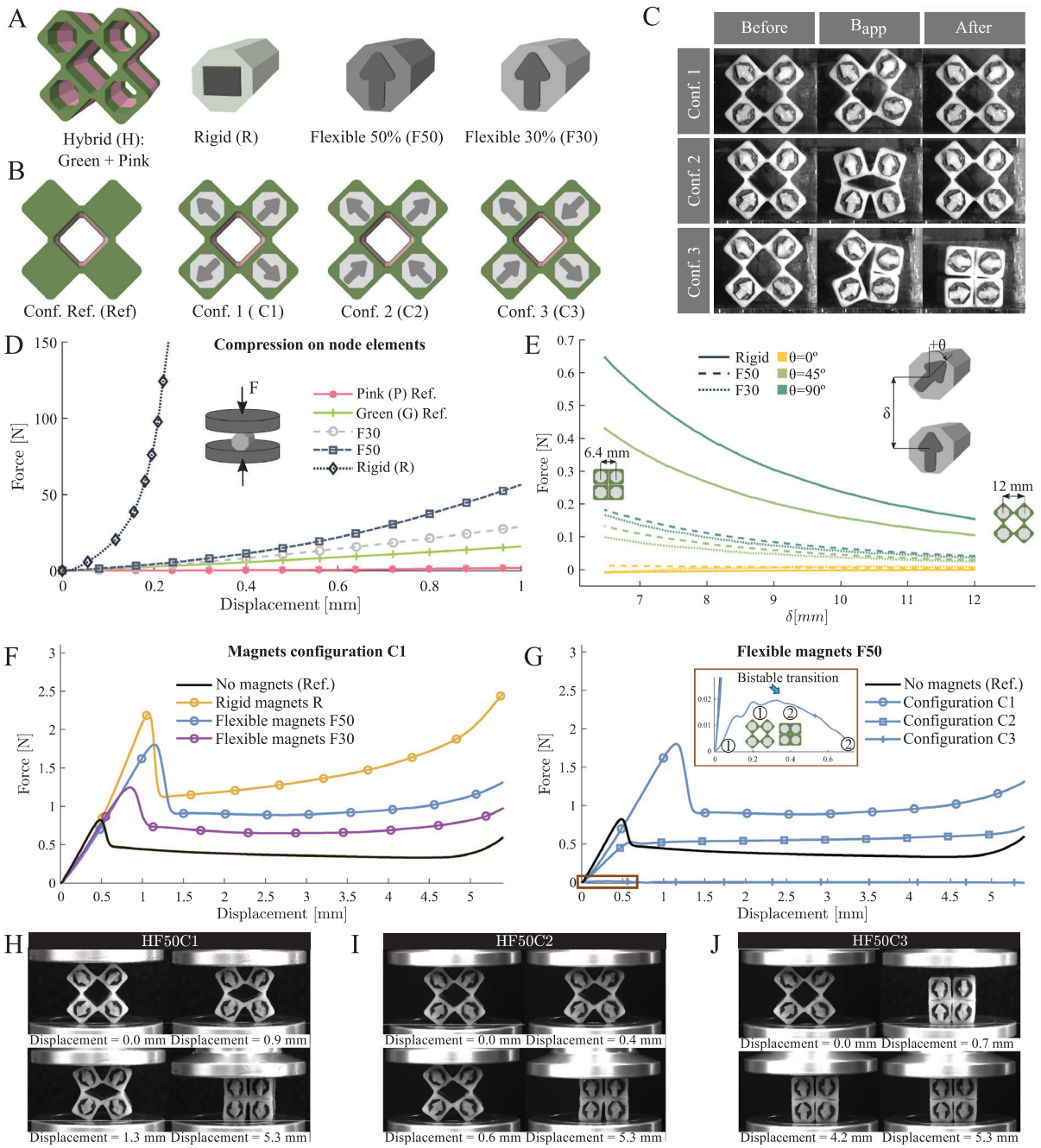

Figure 1. Mechanical and structural response of magneto-responsive unit cells. A) Metastructure matrix and magnetic nodes. Rigid magnets refer to commercial Nd magnets; F50 refers to hard-magnetic magnetorheological elastomers (hMRE) with 50% volume ratio of Nd micron-size particles; and F30 refers to hMREs with 30% volume ratio. B) Unit cell configurations considered in this study with the relative position of the magnetic nodes. The arrows within the nodes indicate the direction of the residual magnetization. A reference case is included with null magnetization in the nodes. C) Structural transitions in the unit cell configurations under a vertical homogeneous magnetic field of 50 mT (B_{app}). The images show the nodes arrangement before, during, and after the application of the magnetic field. D) Transverse compression tests on different node elements: non-magnetic node made of pink material (Pink Ref.); non-magnetic node made of green material (Green Ref.); F30 magnetic node; F50 magnetic node; rigid (R) magnetic node. E) Characterization of the magnetic nodes force interaction depending on the material used (i.e., rigid, F50 or F30) and the relative angle between their residual magnetization directions. This characterization covers the range of distance between magnetic nodes observed during the deformation of the unit cell. F) Force–displacement curves using hybrid matrix material and configuration C1 at the variation of the type of magnetic nodes. G) Force-displacement curves using the hybrid matrix material and magnetic nodes F50 and changing the nodes' configuration. H–J) Imaging frames of the deformation process of the experiments plotted in panel (G). The nomenclature used follows HBC, with H the matrix material used (hybrid), B the magnetic nodes used (R, F50, or F30), and C the magnetic nodes' configuration used (C1, C2, or C3). The reference case relates to the structure with hybrid material and non-magnetic nodes. All experimental curves presented are the mean curves from three replicates. Additional results using the green and pink matrix materials are provided in *Supporting Information*, Figure S3.

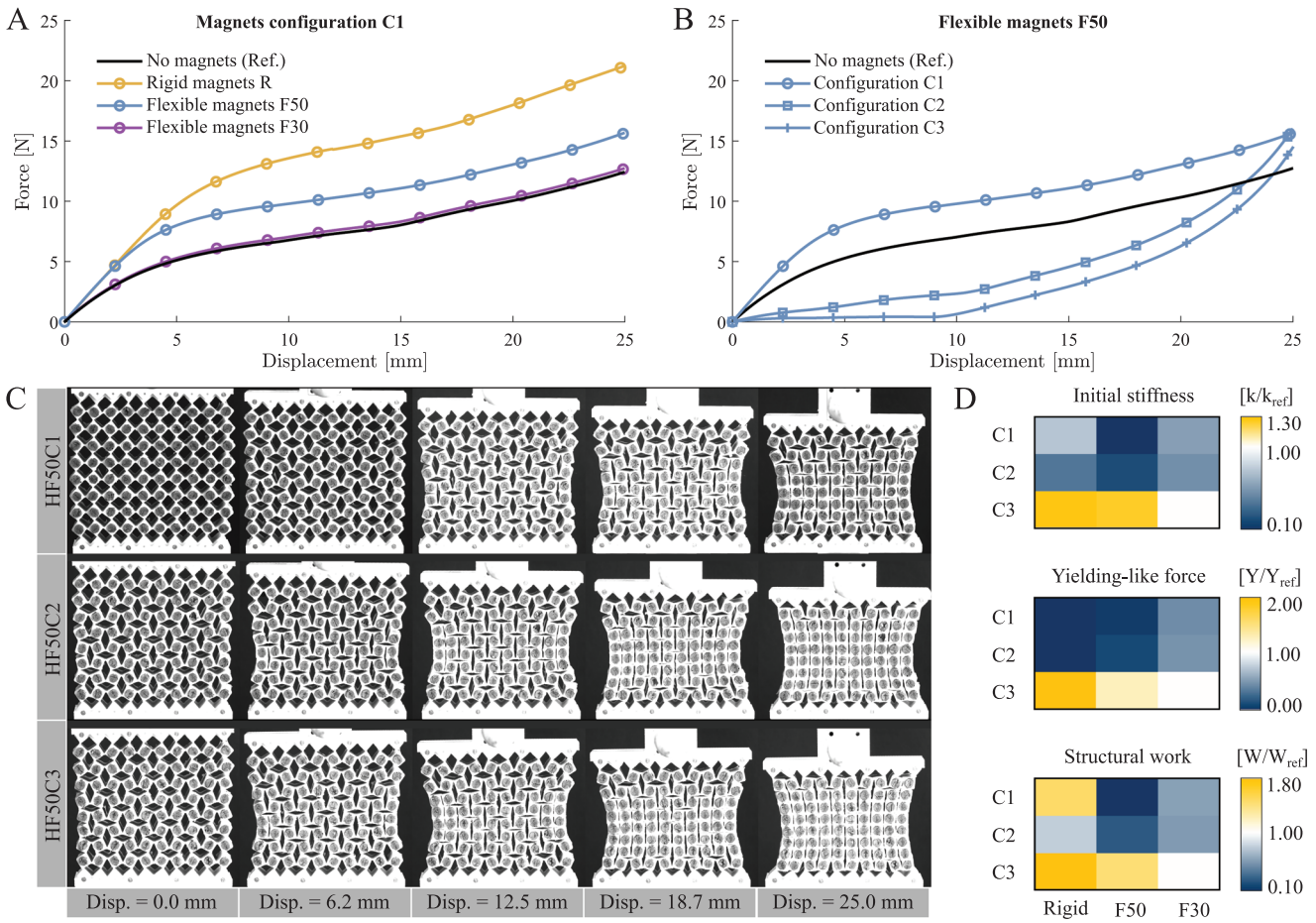

Figure 2. Static response of large magneto-responsive metamaterials. A) Force-displacement curves using hybrid matrix material, fixing the magnetic nodes configuration (C1) and changing the type of magnetic nodes. B) Force-displacement curves using the hybrid matrix material, fixing the magnetic nodes (F50) and changing the nodes' configuration. The reference case relates to the structure using non-magnetic nodes made of the same metastructure matrix material. All experimental curves presented are the mean curves from 3 replicates. C) Imaging frames of the deformation process of the metastructure used in panel B) at different stages. The nomenclature used follows HBC, with H the matrix material used (hybrid), B the magnetic nodes used (R, F50, or F30), and C the configuration of the magnetic node used (C1, C2, or C3). D) Color maps for the hybrid matrix material showing the effects of the type of magnetic nodes and their configuration: (top) initial structural stiffness (k); (middle) yielding-like force (Y); (bottom) structural work (W) until reaching an 8% engineering strain deformation. Note that these results have been normalized with the values obtained for the reference case. Additional results with green and pink matrix materials are provided in *Supporting Information*, Figures S4 and S5.

more rapidly compared to configurations with flexible magnets. Finally, it is also important to note not only the residual magnetization but also the stiffness of the magnets influence the mechanical response of the unit cell when the applied displacements are large enough to cause contact between the squares (*Supporting Information*, Figure S2).

Next, to investigate the effect of magnets orientation, we compare the force-displacement curve for the unit cell with flexible magnets F50 arranged in the three considered configurations (Figure 1G). We find the mix of repulsive and attractive interactions of configuration *C2* results in a behavior close to that of the unit cell without magnets. By contrast, for *C3* the attractive forces result in a transition to a stable compact state under the application of a small displacement of ~0.6 mm. Note that such transition to a stable compact state in the case of a unit cell made of a softer elastomeric material is observed even in the absence of external mechanical loading (see *Supporting Information*, Figure S3, for additional results for unit cells made of different materials).

2.2. From Reprogrammable Unit Cells to Large Metastructures

The results in Figure 1 demonstrate the ability to tailor the mechanical response of the unit cell by adjusting the stiffness, residual magnetization, and orientation of the magnets within the squares. However, this mechanical tunability cannot a priori be assumed in larger structures composed of multiple unit cells, due to the significant influence of periodicity, boundary conditions, and multidomain magnetic interactions. Therefore, we next investigate the behavior of a larger structure consisting of a 10 × 8 array of squares, each with a magnet positioned in the center. In **Figure 2**, we present results from quasi-static uniaxial tests on the metamaterial, with magnets in each 2 × 2 unit cell

oriented according to configurations *C*1, *C*2, and *C*3. Specifically, in Figure 2A, we focus on configuration *C*1 and compare the response of the structure with both rigid and flexible magnets. Similar to the unit cell behavior, under compression, the magnets rotate, generating repulsive forces that resist deformation and cause structural stiffening. However, in this larger structure, the solid material strips at the top and bottom boundaries, added to facilitate loading, introduce constraints and increase the overall structural stiffness. The weaker magnetic interactions produced by the flexible F30 magnets are insufficient to overcome such boundary constraints, resulting in a response nearly identical to the reference structure without magnets. In contrast, the stronger magnets (rigid and F50), unlike in the unit cell, result in a higher initial linear stiffness in the larger structure. This is due to the synergistic interactions between the magnets in the array of unit cells, which amplify the repulsive forces at the structural level.

Next, in Figure 2B we compare the response of the metamaterial with flexible F50 magnets arranged in the three different configurations. For both configurations *C*2 and *C*3, we observe that the attractive forces between the magnets cause a rapid transition to a compact state, similar to what seen in the unit cell with *C*3 under a small mechanical force (Figure 1G). However, for the larger structure, the synergistic attraction between the magnets (i.e., magnetic interactions within unit cells and between cells) enables the structure to transition to its compact state without the need for any external force, resulting in a J-shaped stress–strain response.

To summarize, our findings indicate that the magnetic interactions within the metamaterial result in a 138% modulation in stiffness, a 210% increase in buckling force, and an 181% enhancement in structural work capability under quasi-static loading compared to the structure without magnets (see Figure 2D). While Figure 2 shows the ability to modulate the mechanical response using passive magnets with residual magnetization, this behavior can be further refined by adjusting the balance between elastic and magnetic interactions (see *Supporting Information*, Figures S4 and S5, for results regarding structures made of both stiffer and softer matrix materials).

2.3. Active and Passive Reprogrammable Impact Response

In Figure 2, we demonstrated the remarkable modulation capabilities of magnetic interactions within metamaterials under quasi-static loading. However, it is also important to highlight that these interactions can be harnessed to tune and reprogram the response under dynamic impact, where the evolution of magnetic forces occurs more rapidly. To assess the tunability of our metamaterial's response under impact loading, we used the drop-weight-tower system schematically illustrated in **Figure 3A** (see also *Supporting Information*, Figure S6). This setup features front and back transparent panels with minimum friction that prevent out-of-plane buckling. Impact experiments were carried out using a 0.223 kg impactor, dropped from a height of 19 cm above the sample's top surface, providing an initial kinetic energy of $K_0 = 0.42$ J. The tests were recorded with a high-speed camera, and the impactor's velocity was extracted from the videos to compute the evolution of its kinetic energy over time. Additionally, the entire setup was placed within magnetic coils capable of generating homogeneous magnetic fields up to 50 mT throughout the space (see *Experimental Section* for further details).

In Figure 3B, we present the evolution of the normalized kinetic energy K/K_0 for the metamaterial featuring both rigid and flexible magnets, arranged according to configuration *C*1. In the plot, the contact between the impactor and the structure is set to occur at time $t = 0$, and we track the evolution of K such that the last point on the curves represents the moment when the impactor returns to the height of the initial contact. Therefore, the energy dissipated during the first rebound can be calculated as $K(t = 0) - K(t_l)$, where t_l denotes the last time point in the plotted data. For configuration *C*1, the type of magnets has a more moderate impact on the dynamic response compared to their impact under quasi-static loading. Specifically, the arrest time of the impactor (i.e., the time at which its kinetic energy vanishes) is minimally influenced by the magnet type, whereas stronger modulation is observed in terms of the energy dissipated during the impactor's first rebound. Under dynamic conditions, in addition to the hinge stiffness and the spatially heterogeneous evolution of the magnetic interactions, inertial effects play a critical role. The choice of magnets influences not only the strength and nature of the magnetic interactions but also the contribution of inertial forces. An increase in residual magnetization is associated with higher neodymium content, which increases the mass. In large structures, the energy absorption capacity is determined by the complex interplay between these inertial effects and the magnetic forces.

Next, in Figure 3C we compare the evolution of K/K_0 for the metamaterial with flexible magnets F50 arranged according to configurations *C*1, *C*2, and *C*3. In configurations *C*2 and *C*3, the attractive magnetic interactions compact the structure, leading to significant stiffening from the moment of initial contact at the cost of reduced structural deformability. In configuration *C*3, this stiffening effect causes a marked reduction in both arrest time and energy dissipation compared to configuration *C*1. Interestingly, in configuration *C*2, the combination of magnetic attraction forces along the loading direction and repulsive forces in the transverse direction results in a similar reduction in arrest time, but without significantly altering the energy absorption compared to *C*1. The complete set of dynamic tests for the hybrid structure combining magnets type and configurations is presented in *Supporting Information*, Figure S7. Overall, the results show a modulation capability of 75% in impactor arrest time, and of 37% in energy absorption.

The dynamic response of the metamaterial can be further manipulated by introducing an external magnetic field. In Figure 3D, we present the effect of external magnetic actuation with 50 mT on the large structure with flexible magnets F50 nodes, before impact. For configuration *C*1, the large metastructure, as the unit cell, experiences internal stresses caused by magnetic torques attempting to align the residual magnetization of the nodes with the downward magnetic field. These torques induce slight rotations. However, the initial distribution of residual magnetization in the four beams leads to a balance, resulting in minor deformations in the structural shape. For configuration *C*2, the magnets rotate to align with the external magnetic field, introducing stronger magnetic interactions due to synergistic effects between unit cells that results in a compact

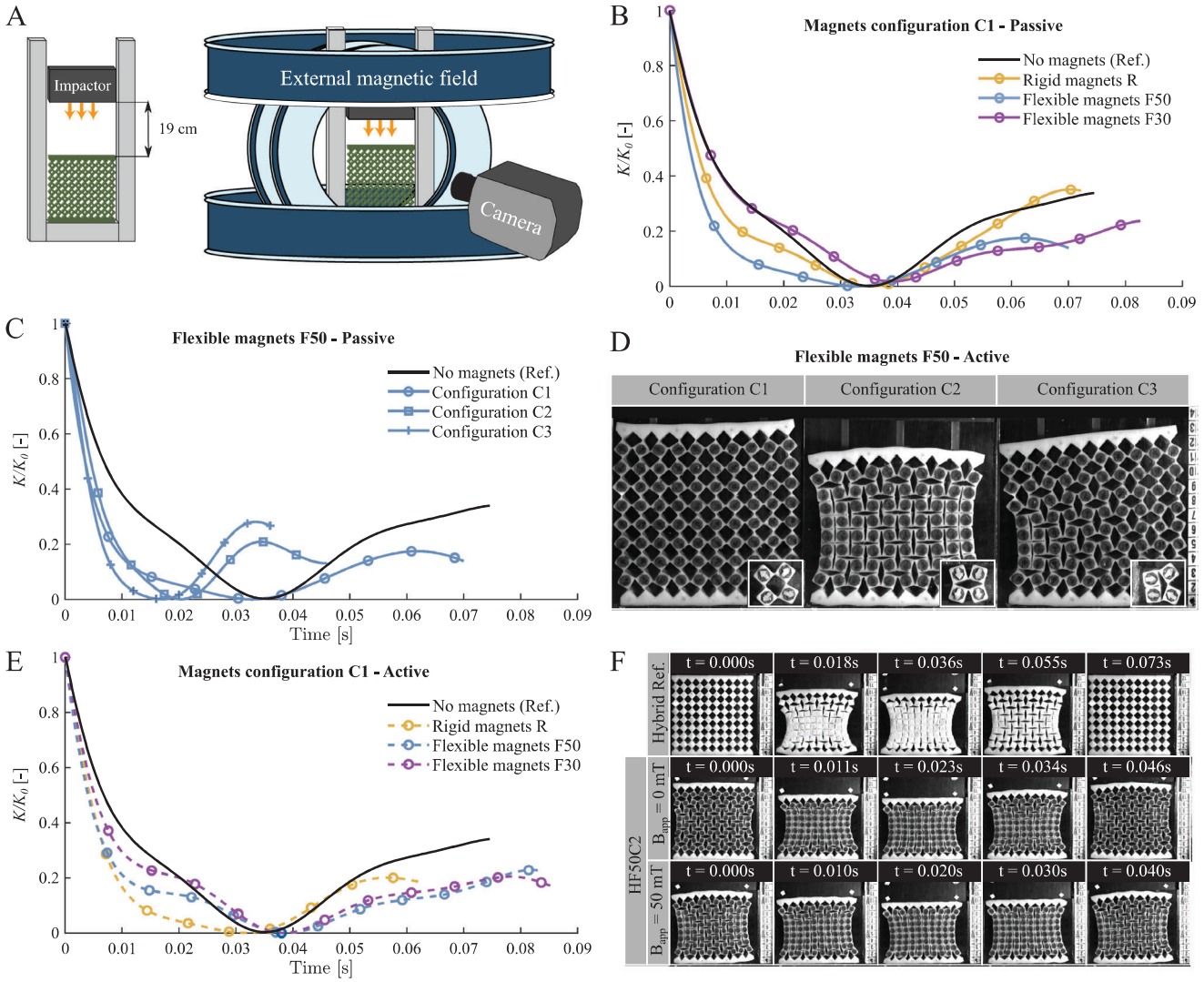

Figure 3. Active and passive reprogrammable impact response. A) Schematic of the drop-weight-tower system implemented for the impact tests on the designed magneto-responsive metastructures, and its coupling with a magnetic field generator and recording system. The magnetic actuation has been restricted to the axial direction of the structure, i.e., aligned with the loading direction. B) Normalized kinetic energy-time curves using the hybrid material with configuration C1 for different types of magnetic nodes under null magnetic actuation. C) Normalized kinetic energy-time curves using the hybrid material and the F50 magnetic nodes for different magnetic nodes' configurations under null magnetic actuation. D) Structural transitions, before impact, in the metastructure with hybrid matrix and F50 nodes under 50 mT magnetic actuation for the different configurations (C1, C2, and C2). E) Normalized kinetic energy-time curves using the hybrid material and the magnetic nodes configuration C1 for different types of magnetic nodes under 50 mT magnetic actuation. The kinetic energy has been normalized with respect to the value at the first contact between the impactor and the structure, which is kept constant for all tests. The nomenclature used follows HBC, with H the matrix material used (hybrid), B the magnetic nodes used (R, F50, or F30), and C the magnetic nodes' configuration used (C1, C2, or C3). The reference case relates to the structure using non-magnetic nodes made of the same metastructure matrix material. All experimental curves presented are the mean curves from 3 replicates. F) Imaging frames of the deformation process of the hybrid metastructure with F50 nodes in configuration C2 under null and 50 mT actuation, along with the reference case. Note that representative movies of impact tests are provided in *Supporting Information*. Note that all experiments are conducted analyzing the first impact, which is also representative of the subsequent impacts.

structural state. Finally, in configuration *C*3, the antimetric distribution of the magnetic nodes causes one side of the structure to compact while the opposite side extends, similar to the behavior observed at the unit cell level. Although the deformation mode scales from the unit cell to the larger metastructure, the final distribution of the magnets' residual magnetization differs in both cases due to the distinct boundary conditions in each scenario.

In Figure 3E, we conducted the same experiments presented in Figure 3B but applying a homogeneous magnetic field of 50 mT along the impact direction within the whole space occupied by the structure. The evolution of the kinetic energy during the impact test is altered under the presence of the external magnetic field applied. The strongest difference is observed for the use of rigid magnets with stronger residual magnetization. Under external magnetic actuation, the arrest time is

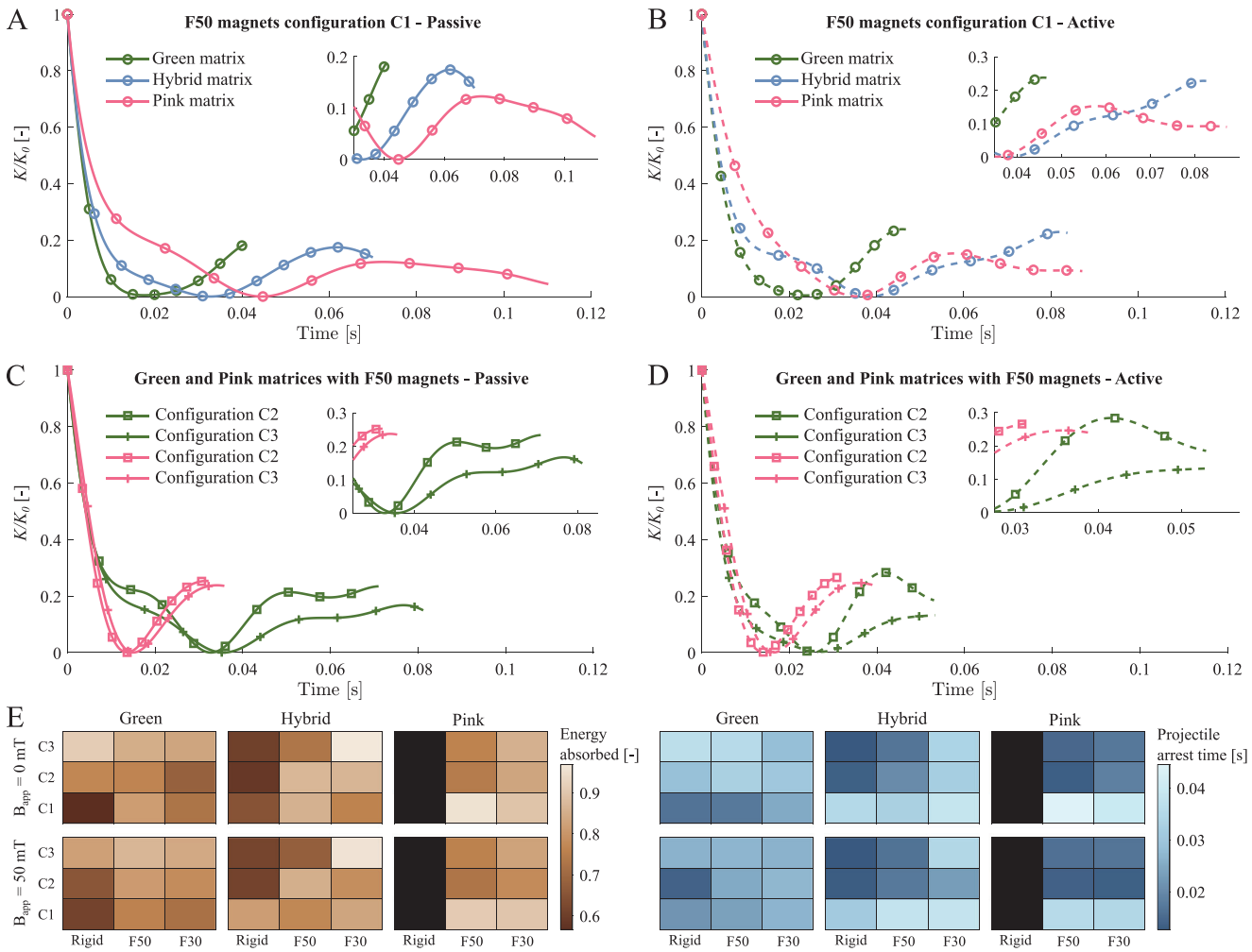

Figure 4. Influence of the matrix stiffness on the active and passive impact response. A,B) Kinetic energy-time curves using F50 magnetic nodes and the magnetic configuration C1, for the green (G), the hybrid (H), and the pink (P) matrix materials under null and 50 mT magnetic actuation, respectively. C,D) Kinetic energy-time curves using F50 magnetic nodes and the magnetic configurations C2 and C3, for the green (G) and the pink (P) matrix materials under null and 50 mT magnetic actuation, respectively. The kinetic energy has been normalized with respect to the value at the first contact between the impactor and the structure, which is kept constant for all tests. All experimental curves presented are the mean curves from 3 replicates. E) Color maps for the three metastructure matrix materials considered in this work showing the effects of the type of magnetic nodes and their configuration, under both null and 50 mT magnetic actuation, on energy absorption (brown color scale) and impactor arrest time (blue color scale). Note that these results are computed from the normalized kinetic energy. The results indicated in black represent those configurations where the magnetic nodes induced structural collapse. All experiments are conducted analyzing the first impact, which is also representative of the subsequent impacts.

reduced (from 0.0354 to 0.0316 s) and the energy absorbed is increased. The introduction of an external magnetic field can alter the strength of the magnetic interactions between magnets and create additional interactions between nodes and the background field. This leads to structural stiffening due to the extra resistance of the nodes to rotate within the background field (i.e., due to Zeeman effects). The dynamic tests for different magnetic configurations under external magnetic actuation are provided in *Supporting Information*, Figure S8. These tests demonstrate an overall structural stiffening that leads to a reduction in both impactor arrest time and energy absorption in most cases.

To further understand the interplay between elastic and magnetic interactions, we changed the elastomeric material used to fabricate the structures, while keeping the same magnets. In particular, we conducted the same tests as in Figure 3 but in structures made of Green Zhermack Elite Double 32A (stiffer) and Pink Zhermack Elite Double 8 (softer). First, we evaluated the role of matrix stiffness on the passive response of large metastructures under impact conditions using configuration C1 and F50 magnets (**Figure** 4A). Stiffer materials present steeper curve slopes leading to shorter projectile arrest times, with the system reaching a state of null kinetic energy faster (quantitative evaluation in Figure 4E). The rebound time, when the projectile reaches the initial height at contact, is also minimized for stiffer matrices. In contrast, the use of softer matrix materials delays both impactor arrest time and rebound time due to higher compliance of the structure. This higher structural deformation also introduces higher energy dissipation for configuration C1 for softer matrices (quantitative evaluation in Figure 4E). The same tests were

then conducted on large metastructures using configuration *C*1 but under external magnetic actuation of 50 mT (Figure 4B). The capacity of the metastructure to dissipate energy during the projectile rebound decreases for all stiffness matrices under external magnetic actuation (quantitative evaluation in Figure 4E). This effect can be explained by the non-dissipative nature of the magnetic interactions and the negligible structural changes magnetically induced in configuration *C*1 (see Figure 3D). The magnetic actuation generates conservative strong interactions between the magnetic nodes and the actuating field, diminishing the relative contribution of the passive mechanical response of the metastructure and leading to a more uniform overall behavior. These effects lead to projectile arrest time decreases in the softer matrix (pink) but increases in the stiffer matrix (green).

The influence of matrix stiffness for configurations *C*2 and *C*3 under impact loading was evaluated under passive conditions (Figure 4C). The use of a softer matrix (pink) causes a structural collapse for configurations *C*2 and *C*3 due to insufficient mechanical resistance, resulting in a significant decrease in both projectile arrest time and energy absorbed with respect to configuration *C*1. Note that this structure presents structural collapse even in the absence of external loading. Although the experiments conducted only focus on the first impact, the ability of these structures to absorb energy will be the same for subsequent impacts, and peak loads will decrease as a result of the lower kinetic energy of the impactor. For the stiffest material (green), the magnetic interactions for configurations *C*2 and *C*3 between nodes induce structural softening exhibiting an increase in flexibility, as indicated by the change in slope before reaching null kinetic energy. This change in behavior delays the arrest time and enhances the energy absorption capability. The shape of the metastructure, and thus its impact performance, also remains the same before and after impact when using configuration *C*3 with this stiffer material, in this case in a non-collapsed state. We collect the corresponding impact experiments for configurations *C*2 and *C*3 under magnetic actuation in Figure 4D. The magnetic field for these configurations introduces a structural stiffening that, for the use of the softest matrix (pink) where the metastructure is partially collapsed in a compacted state, does not significantly alter the response to impact loading. For the stiffest material (green), the external magnetic field introduces a shift in the magneto-mechanical balance leading to a compacted metastructure state. This structural change reduces the projectile arrest time and enhances the energy absorption capability.

Dynamic tests were performed for all combinations of matrix material, magnetic nodes, and configurations. Those results can be found in *Supporting Information*, Figures S7 and S8. An overall picture of all test conditions is provided in Figure 4E in terms of projectile arrest time and energy absorption. The experiments show a passive modulation capability of 91% and 85% in impactor arrest time, and of 35% and 20% in energy absorption for the green and the pink structures, respectively. Regarding the modulation capability through external magnetic actuation, the results show changes of 51% and 20% in impactor arrest time, and of 15% and 7% in energy absorption for the green and the pink structures, respectively.

2.4. Decoupling Static and Impact Response Via Spatial Magnetic Modulations

All previous experiments considered homogeneous spatial distributions of unit cell configurations (Figures 2–4). These results showed the great capability of the proposed magnetic metastructures to design the mechano-structural response of the component. Interestingly, the multi-compartment design of the metastructure allows for reprogramming the magnetic nodes distribution, thus modulating the response against quasi-static and dynamic loading conditions. Homogeneous spatial distributions have been demonstrated to change the quasi-static and dynamic behavior modulating the energy absorption capability of the structure, its stiffness and strength magnitudes as well as the impactor arrest time. These characteristics open new avenues to conceptualize reprogrammable structures subjected to both static and dynamic conditions. However, some scenarios may require modulation of the structural response under a specific loading condition without significantly altering the referential response to another loading condition.

Here we pose the question of whether heterogeneous distributions of magnetic nodes may modulate the structural behavior only for quasi-static or dynamic conditions without altering the response to the other case. To explore this, we considered four heterogeneous distributions that combine unit cell configurations *C*1 and *C*3 (see **Figure** 5A). These two unit cell configurations were chosen because they introduce opposite magnetic interactions between nodes, i.e., repulsive forces with configuration *C*1 and attraction forces with configuration *C*3. These new metastructures were tested under static and dynamic loading. The results for quasi-static tests are collected in Figure 5B whereas those for dynamic impact tests are collected in Figure 5C. The corresponding experiments for the reference case and homogeneous magnetic nodes with configurations *C*1 and *C*3 are represented for comparison. Note that, under quasi-static conditions, the structural response is determined by the total interplay between magnetic nodes interactions. However, dynamic loading introduces strong inertial terms that give rise to notable local differences in the rotational speed between magnetic nodes, altering such an interplay. Therefore, we predict that the combination of unit cells may lead to changes under static loading and not under dynamic loading, and vice versa. In this regard, configuration 1313 presents a mechanical response very similar to that of the reference (i.e., non-magnetic) case for quasi-static loading but a significantly modulated response under dynamic loading in terms of arrest time. This can be explained by the stiffening role of configuration *C*1 and the softening role of configuration *C*3 on the structural response. When these configurations are alternated by rows, the stiffening and softening contributions are balanced. Note that these regions present stronger stiffness irrespectively of the magnetic nodes configuration due to boundary conditions, being their contribution weaker than that of the central region of the metastructure. For configuration 1313, the structure features a stiffening component in the upper gripping site and a softening component in the lower one. Under dynamic loading, however, the heterogeneous local deformations due to inertial effects break this balance leading to a change in mechanical response. The opposite case is found for configuration 1331, with modulation under quasi-static conditions and no changes

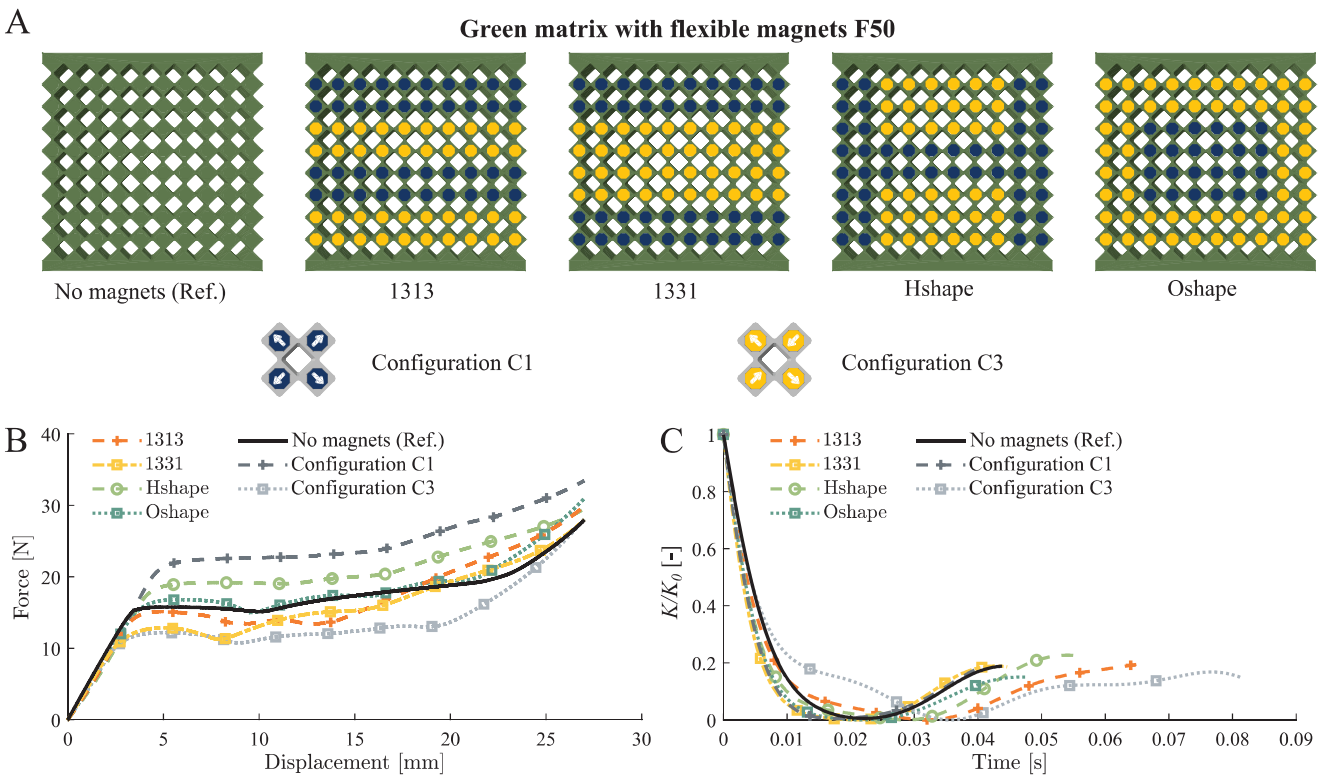

Figure 5. Effect of spatial magnetic modulations on the static and impact response. A) Non-homogeneous unit cell distributions considered: 1313, 1331, Hshape, and Oshape. The green (G) matrix material and F50 magnetic nodes have been chosen for all conditions. The configurations are based on spatial distributions of configuration *C*1 (blue nodes) and configuration *C*3 (yellow nodes) unit cells. B) Force-displacement curves under uniaxial quasi-static loading for all configurations considered. C) Kinetic energy-time curves under dynamic impact loading for all configurations considered. The reference cases are included in black and relate to the structure using non-magnetic nodes made of the same metastructure matrix material. The results for the previous experiments using homogeneous unit cells configurations are added in gray. All experimental curves presented are the mean curves from 3 replicates.

in mechanical response under dynamic loading. In this case, both repulsive configuration rows are located in the gripping regions. This explains the softer response under quasi-static conditions. Under dynamic loading, on the contrary, the local stiffening and softening contributions are balanced for this structural arrangement. Finally, the Oshape configuration introduces structural balance under static and dynamic loading scenarios, and the Hshape provides modulation in both cases. Note that the stiffness of the matrix material used for the metastructure plays an important role in this modulation. Overall, we appreciate that, under impact loading, the inertial terms play a consistent and significant role across all conditions, diminishing the relative effect of magneto-mechanical coupling. These terms are especially crucial during the compression phase, continuing to influence the system until impact arrest. When the distribution of repulsive and attractive unit cells is altered but maintains a similar relative unit cell density (i.e., the proportion of *C*1 to *C*3 unit cells), the inertial terms predominantly govern the dynamic response, resulting in similar energy-time behavior. However, when using homogeneous distributions of either repulsive or attractive unit cells alone (e.g., only *C*1 or only *C*3), the observed behavior undergoes considerable modulation. Following impact arrest, the influence of the inertial terms decreases significantly, shifting the dynamic response during the rebound phase to be governed by the absorbed elastic (mechanical) component and the magneto-mechanical coupling. In this rebounding stage, distinct energy-time modulation is observed, even for the previously mentioned cases. While the relative modulations observed with the stiffer material (green) remain consistent under quasi-static loading, when using a softer matrix notable changes occur under dynamic loading (*Supporting Information*, Figure S9). These differences are attributed to the increased compliance of the softer matrix, which amplifies the relative contributions of inertial effects and their interplay with the evolution of the magnetic interactions between nodes.

3. Discussion

Here, we investigated the reprogrammable behavior of mechanical metamaterials via magnetic interactions. We showed that by distributing permanent magnets with strategically chosen orientations within the structure, we can significantly modulate the quasi-static *and* dynamic structural behavior. Additionally, external magnetic actuation can be employed to further enhance structural tunability. A key advantage of our proposed method is the ease of reconfiguring the magnets, which leads to substantial changes in the structural response. In this regard, the magnets

can be extracted from the structure without taking it apart, only requiring an accessible face.

This work demonstrates the concept and the potential of these structures to modulate key mechanical features such as structural stiffness, maximum force capacity, energy absorption capability, and nonlinear response. Additionally, it identifies new challenges for future research: the ability to configure and reconfigure structural responses to geometrically heterogeneous loading, and the development of computational optimization tools to guide the magnetic configuration of the structure. The computational modeling of this problem is especially challenging due to the numerous nonlinear and multiphysics mechanisms involved. Discrete models that combine mechanical and magnetic springs to connect magneto-responsive nodes offer an efficient route to optimization. However, these models are limited to rigid body motion of the nodes, which restricts their use to stiff structures—making them less suitable for applications in soft robotics and energy absorption. Finite element models represent an alternative to describe large deformations of the structure and its soft components. The main challenges with this approach stem from the need to incorporate the surrounding air domain that connects the magnetic nodes.[50,51] This step is crucial for solving the magnetic problem and accounting for the force and torque interactions between nodes due to residual magnetization. However, it also introduces significant computational cost, hindering the efficiency of optimization methods. In light of these challenges, this work provides indispensable experimental evidence and guidance for the development of future inverse-design strategies, which will need to strike the balance between low-dimensional discrete models and full-field finite element approaches. In addition, the fabrication and experimental methods here introduced can readily be deployed for efficient data collection to power data-driven optimization strategies for specific applications.

These magneto-responsive structures also present significant opportunities for tunable damping components and protection against impact loading. The reconfigurable nature of these metastructures allows for the optimization of the mechanical response to a specific loading condition, followed by reoptimization for entirely different loading scenarios. These structures offer two modulation options: fast modulation through external magnetic actuation and slower modulation via the redistribution of magnets. This concept paves the way for damping systems that can adapt to varying conditions. For instance, these components could be beneficial for exoskeletons that need to accommodate different loads in magnitude and rate depending on the situation. They could also be used in the soles of training shoes to better accommodate forces generated during different activities, such as walking or running. Note that we used a large experimental setup to ensure a perfectly homogeneous magnetic field to facilitate the analysis of magneto-mechanical coupling in large metastructures. However, the actuating fields generated were relatively low, below 50 mT. These low-field intensities can be achieved using Nd magnets and simplifying the actuation system, but losing precise control of spatial actuating heterogeneity. In practical applications, electromagnetic systems with iron cores or less homogeneous fields could still yield equivalent responses by redistributing magnetic nodes to offset any heterogeneous coupling effects. In contrast, structures fully composed of magnetorheological elastomers lack mechanical reprogrammability without complex systems that involve melting the matrix, reorienting magnetic fillers, and recurring the composite. These processes incur notable time and cost limitations, and the passive modulation achievable in such systems is significantly lower than what we demonstrate here.

Additionally, we have demonstrated the capability to reprogram the mechano-structural behavior of these components, allowing modulation of their response to both static and dynamic loading or even isolating the modulation to a specific loading case. This advancement has the potential to motivate future solutions for reconfigurable mechano-structural applications, enhanced by the addition of magneto-responsive remote actuation.

4. Experimental Section

Materials and Manufacturing Methods for Rigid Magnetic Nodes: Rigid magnetic nodes were manufactured considering two different parts. In its center, neodymium N48 magnets (SUPERIMANES, Sevilla, Spain) with dimensions 20 mm length (coinciding with the metastructure depth), 4 mm width and 3 mm height are placed. These magnets are magnetized along the height direction. Surrounding them, components with external octagon shape with radius 3.5 mm and an internal cavity with the same dimensions as the neodymium magnets. Durable resin and Form 3+ printer from Formlabs Inc. were used for printing them with layer height of 0.1 mm. The octagon components were washed with isopropyl alcohol (IPA) after the printing process during 10 + 10 min and cured during 10 min at 60°C, following Formlabs Inc. settings for these procedures.

Materials and Manufacturing Methods for Flexible Magnetic Nodes: Flexible magnetic nodes were manufactured using rubber-like elastomer (Elite Double 32, Zhermack) and hard-magnetic particles consisting of micron-size Nd-FeB powder (MQP-S-11-9 grade powder, Neo Materials Technology Inc., Greenwood Village, Colorado, United States). This elastomer was used to provide a similar stiffness to that of the matrix metastructure where the nodes were located, and to prevent rotation of the micron-size particles due to local magnetic torques. The pre-cured elastomer is composed of two components (i.e., base and catalyst) that were mixed in 1:1 ratio. The manufacturing process consists in mixing the elastomer base with magnetic particles previously weighted to obtain a final mixture with 30% or 50% volume ratio of magnetic particles. After mixing these two components, elastomer catalyst was added to initiate the cross-link of the phases. Then, it was poured into a 3D printed mold with 100 cavities with 20 mm depth and octagon shape cross-section of 3.5 mm radius. To facilitate the entry of the material into the mold, vacuum was applied for 20 s. This mold was printed using SLA technique and Form 3+ printer from Formlabs Inc. and Draft resin with layer height of 0.1 mm. The mold was later cleaned for 10 min, following Formlabs Inc. setting and cleaned again by hand with IPA to avoid non-cured resin remnants that could interact with the pre-cured elastomer mixture. No curing process was applied to the component. The final step involved pre-magnetizing the hMRE by placing it into an impulse magnetizer (DXMM-12C40 Magnetizer, Dexing Magnet Tech. Co., Limited, China) and applying a homogeneous magnetic field of 3 T, which exceeds the magnetization saturation of the particles.

Materials and Manufacturing Methods of Unit Cell and Lattice Structures Mold: The structures developed in this work were motivated by the geometrical design provided in Ref. [19]. They were manufactured using molding techniques and considering three different mold parts, all of them printed using a Form 3+ from Formlabs Inc. The mold base was printed using Draft resin with layer height of 0.1 mm and following the same cleaning process defined in the previous section. This part defines the external shape of the molded structure and contains cavities to generate lattice structural shape. The molds were manufactured using Durable resin V2 from Formlabs Inc., cleaned using a washing process in IPA and cured for

60 min at 60°C. Further details on the molds used to manufacture these components are provided in *Supporting Information*, Figures S10– S14.

Material and Manufacturing Methods for Material Characterization Specimens: For the mechanical characterization test, specimens with dimensions 50 mm length, 4 mm thickness, and 7 mm width were considered. These specimens were manufactured using two materials with different stiffness (Green-Elite Double 32 and Pink-Elite Double 8) and the layered combination of them considering a Green-Pink mixing volume ratio 1:1 for the Hybrid specimens. These materials were chosen because of their low viscoelastic behavior, which allows to simplify the problem to elastic contributions from the metastructure matrix. The precured elastomer was composed by two components as defined in Section Materials and Manufacturing Methods for Flexible Magnetic Nodes. Green and Pink structures were manufactured by mixing the base and catalyst with mixing ratio 1:1 and introducing it into a syringe. The mixture was then expelled using an air compressor until the whole model is filled. This process allowed to control the amount of elastomer added and prevented the appearance of air at the bottom part between the elastomer and the mold. A similar process was used for the Hybrid specimen but considering a multi-step manufacturing process. These specimens were composed of three different layers of 1, 2, 1 mm thickness each respectively, using the Green-Elite Double 32 for the exterior layers.

Materials and Manufacturing Methods of Unit Cell and Lattice Structures: These structures were manufactured using the same molding techniques and the materials (Green, Pink and Hybrid) described for the specimens, For the Hybrid structure the multi-step manufacturing process was used considering three different layers of 5, 10, 5 mm thickness each respectively, using the Green-Elite Double 32 for the exterior parts. To do this, the volume of each layer was measured with a CAD model.

Experimental Procedure to Characterize the Magnetic Forces Between Nodes: For all the three magnetic node types used in this work, the same experimental procedure was devised using a universal testing machine (INSTRON 34TM-5, MA, USA) equipped with a 50 N load cell and INSTRON grips. For each type, two nodes were taken placing one in the moving grip and the other in the fixed one. After closing the grips, the node located in the moving grip is approached to the fixed one until they are in contact. The test consisted in moving away one node at a rate equal to 0.05 mm/s while measuring the force in terms of the distance between the nodes' center. The relative displacement between magnetic nodes was increased until reaching negligible interaction force.

Experimental Procedure for Mechanical Specimen Characterization: These experiments were performed considering quasi-static uniaxial testing and using a universal testing machine (INSTRON 34TM-5, MA, USA) equipped with a 50 N load cell and INSTRON grips. Each specimen with a total length of 50 mm was placed in the machine grips leaving an effective length on each of 25 mm. Force was tared after closing the upper grips. After closing the lower grip, before starting the test, a settling procedure was started so the testing machine adjusts to zero the initial force after closing the second grips. These tests were performed considering a displacement rate of 0.05 mm/s.

Experimental Procedure for Uniaxial Compression Test of Lattice Unit Cell: All possible unit cells combining the considered metastructure matrix materials, magnetic nodes types and their spatial configurations were tested. A universal testing machine (INSTRON 34TM-5, MA, USA) was used, equipped with a 50 N load cell and compression plates. Lubricant was added to reduce friction at the plates contact.

Experimental Procedure for Uniaxial Compression Test of Lattice Structures: These tests were performed using a universal testing machine (INSTRON 34TM-5, MA, USA) equipped with a 50 N load cell and INSTRON grips. To correctly apply clamped boundary conditions in both upper and lower lattice structures surfaces, a 3D printer part was manufactured using PLA in a Prusa 3D printer. This part allowed to fix the edges of the structure preventing its deformation. For testing, the structure was first fixed using the upper grip and letting it settle before taring the force, because of the magnetic interaction of the nodes. Then, the lower grip was closed and the controlled-displacement test was performed using a rate of 0.05 mm/s.

Experimental Procedure for Impact Testing: The tests were performed using a drop-weight tower specifically developed to hold the specimen and guide the impactor in its fall, with the additional requirements of being able to be housed inside a magnetic field generator and to allow filming using a high-speed camera (see Figure 3A and *Supporting Information*, Figure S6). The tower was made of transparent PMMA to allow filming of the deformation process of the specimen through it. The impactor, made of colored PMMA to allow its visualization during the fall, had a dimension of 139x69x20 mm (width x height x thickness) and a mass of 0.223 kg. It also incorporated markers attached to it to allow position tracking during the test. The distance between the lower face of the impactor at rest and the upper face of the specimen was 190 mm in all tests, imposing the same impact energy in all tests. The impact was filmed using a Photron fastcam SA-Z camera, with maximum resolution 1024x1024 pixels and a frequency of 5000 frames per second, which allows, together with the Tracker tracking software (Open Source Physics), to obtain the time history of the impactor position, as well as to visualize the deformation process of the specimen. Preliminary free-fall tests performed without a specimen verified that the friction between the impactor and the tower is negligible, so that the energy was transmitted between the impactor and the specimen without appreciable losses. The tower was inserted inside a Helmholtz coil (Dexin Mag) which, in active tests, generated a vertical magnetic field of 50 mT. The specimen was placed within the volume of the coil that guaranteed the uniformity of the magnetic field (15 × 15 × 15 cm^3). The complete device finally allowed thedetermining the time evolution of the kinetic energy of the impactor, starting at the onset of contact and ending when the impactor reaches the initial contact height after rebound. In this way, two magnitudes of interest for the design of protection systems were determined: a) the time elapsed from the onset of the contact until the stopping of the impactor, correlated with its average deceleration; b) the energy of the impactor absorbed by the specimen.

Supporting Information

Supporting Information is available from the Wiley Online Library or from the author.

Acknowledgements

The authors acknowledge support from Ministerio de Ciencia e Innovacion MCIN/AEI/10.13039/501100011033 under Grant number PID2020-117894GA-I00, the European Research Council (ERC) under the European Union's Horizon 2020 research and innovation program (grant agreement No. 947723, project: 4D-BIOMAP), and the Catedra UC3M–NAVANTIA–MONODON: DEEPTECH. G.R. acknowledges the Swiss National Science Foundation for funding the project. Project: Metamaterials with reprogrammable shape and stiffness (grant no.: 217901).

Conflict of Interest

The authors declare no conflict of interest.

Data Availability Statement

The data that support the findings of this study are available from the corresponding author upon reasonable request.

Keywords

energy absorption, magneto-mechanics, metastructures, structural reprogrammability

Received: August 20, 2024
Revised: November 11, 2024
Published online: April 16, 2025

[1] Z. Hooshmand-Ahoor, M. Tarantino, K. Danas, *Mech. Mater.* **2022**, *173*, 104432.
[2] L. Hu, Z. Luo, Q. Yin, *Thin-Walled Structures* **2019**, *141*, 283.
[3] X. Chen, M.-H. Fu, W.-H. Li, S. V. Sheshenin, *Adv. Eng. Mater.* **2021**, *23*, 2001491.
[4] P. Soman, D. Y. Fozdar, J. W. Lee, A. Phadke, S. Varghese, S. Chen, *Soft Matter* **2012**, *8*, 4946.
[5] Z. G. Nicolaou, A. E. Motter, *Nat. Mater.* **2012**, *11*, 608.
[6] Y. Yao, Y. Zhou, L. H. Chen, Y. J. Gu, M. Li, X. H. Li, X. Zhao, N. Xu, J. H. Jin, J. Ding, *Compos. Struct.* **2024**, *337*, 118032.
[7] T. Bückmann, M. Thiel, M. Kadic, R. Schittny, M. Wegener, *Nat. Commun.* **2014**, *5*, 4130.
[8] X. Guo, X. Ni, J. Li, H. Zhang, F. Zhang, H. Yu, J. Wu, Y. Bai, H. Lei, Y. Huang, J. A. Rogers, Y. Zhang, *Advanced Materials* **2021**, *33*, 2004919.
[9] C. Coulais, D. Sounas, A. Alu, *Nature* **2017**, *542*, 461.
[10] W. Ye, L. Hu, H. Ou, T. Yu, *Sci. Adv.* **2023**, *9*, eadh3870.
[11] M. Fleisch, A. Thalhamer, G. Meier, I. Raguž, P. Fuchs, G. Pinter, S. Schlögl, M. Berer, *Mater. Today Adv.* **2021**, *11*, 100155.
[12] S. Wang, J. Guo, A. Biczo, N. Feng, *Mater. Des.* **2024**, *241*, 112913.
[13] A. McCrary, M. S. Hashemi, A. Sheidaei, *Adv. Theory Simul.* **2022**, *5*, 2200135.
[14] Y. Zhang, X. Ren, D. Han, X. Cheng, W. Jiang, X. G. Zhang, X. Y. Zhang, Y. M. Xie, *Int. J. Impact Eng.* **2022**, *164*, 104193.
[15] C. Morris, L. Bekker, C. Spadaccini, M. Haberman, C. Seepersad, *Adv. Eng. Mater.* **2019**, *21*, 1900163.
[16] W. Liu, S. Janbaz, D. Dykstra, B. Ennis, C. Coulais, *arXiv preprint arXiv:2310.04748* **2023**.
[17] S. Shan, S. H. Kang, J. R. Raney, P. Wang, L. Fang, F. Candido, J. A. Lewis, K. Bertoldi, *Adv. Mater.* **2015**, *27*, 4296.
[18] S.-Y. Jeon, B. Shen, N. A. Traugutt, Z. Zhu, L. Fang, C. M. Yakacki, T. D. Nguyen, S. H. Kang, *Adv. Mater.* **2022**, *34*, 2200272.
[19] B. Deng, A. Zareei, X. Ding, J. C. Weaver, C. H. Rycroft, K. Bertoldi, *Adv. Mater.* **2022**, *34*, 2206238.
[20] T. Butruille, J. C. Crone, C. M. Portela, *Proc. Natl. Acad. Sci.* **2024**, *121*, e2313962121.
[21] Q. He, S. Ferracin, J. R. Raney, *Nat. Comput. Sci.* **2024**, *4*, 567.
[22] X. Xia, C. M. Spadaccini, J. R. Greer, *Nat. Rev. Mater.* **2022**, 1.
[23] L. M. Korpas, R. Yin, H. Yasuda, J. R. Raney, *ACS Appl. Mater. Interfaces* **2021**, *13*, 31163.
[24] T. Hanuhov, N. Cohen, *Int. J. Mech. Sci.* **2024**, *262*, 108716.
[25] A. Kotikian, A. A. Watkins, G. Bordiga, A. Spielberg, Z. S. Davidson, K. Bertoldi, J. A. Lewis, *Adv. Mater.* **2024**, 2310743.
[26] S. Leanza, J. Lu-Yang, B. Kaczmarski, S. Wu, E. Kuhl, R. R. Zhao, *Adv. Funct. Mater.* **2024**, 2400396.
[27] G. Risso, M. Kudisch, P. Ermanni, C. Daraio, *Adv. Sci.* **2024**, *11*.
[28] Y. Zhu, M. Birla, K. R. Oldham, E. T. Filipov, *Adv. Funct. Mater.* **2020**, *30*, 2003741.
[29] J. Crespo-Miguel, S. Lucarini, A. Arias, D. Garcia-Gonzalez, *npj Comput. Mater.* **2023**, *9*, 134.
[30] E. Palleau, D. Morales, M. D. Dickey, O. D. Velev, *Nat. Commun.* **2013**, *4*, 2257.
[31] X. Zhou, T. Li, J. Wang, F. Chen, D. Zhou, Q. Liu, B. Li, J. Cheng, X. Zhou, B. Zheng, *ACS Appl. Mater. Interfaces* **2018**, *10*, 9077.
[32] X. Xia, A. Afshar, H. Yang, C. M. Portela, D. M. Kochmann, C. V. Di Leo, J. R. Greer, *Nature* **2019**, *573*, 205.
[33] Y. Chen, L. Jin, *Extreme Mech. Lett.* **2018**, *23*, 55.
[34] S. Li, K. Wang, *Smart Mater. Struct.* **2015**, *24*, 105031.
[35] T. Hewage, K. Alderson, A. Alderson, F. Scarpa, *Adv. Mater.* **2016**, *28*, 10323.
[36] R. Galea, K. K. Dudek, P.-S. Farrugia, L. Z. Mangion, J. N. Grima, R. Gatt, *Compos. Struct.* **2022**, *280*, 114921.
[37] A. S. Gliozzi, M. Miniaci, A. Chiappone, A. Bergamini, B. Morin, E. Descrovi, *Nat. Commun.* **2020**, *11*, 2576.
[38] Q. Zhang, J. Wommer, C. O'Rourke, J. Teitelman, Y. Tang, J. Robison, G. Lin, J. Yin, *Extreme Mech. Lett.* **2017**, *11*, 111.
[39] M. Schaeffer, M. Ruzzene, *Int. J. Solids Struct.* **2015**, *56*, 78.
[40] H. Yasuda, L. M. Korpas, J. R. Raney, *Phys. Rev. Appl.* **2020**, *13*, 054067.
[41] S. Qi, H. Yao, J. Fu, Y. Xie, Y. Li, R. Tian, M. Yu, H. Guo, *Compos. Sci. Technol.* **2022**, *230*, 109789.
[42] Z. Zhang, J. T. Heron, A. Pena-Francesch, *Adv. Funct. Mater.* **2023**, *33*, 2215248.
[43] B. Zou, Z. Liang, D. Zhong, Z. Cui, K. Xiao, S. Shao, J. Ju, *Adv. Mater.* **2023**, *35*, 2207349.
[44] V. Slesarenko, *Materials* **2020**, *13*, 1313.
[45] K. Bertoldi, P. M. Reis, S. Willshaw, T. Mullin, *Adv. Mater. (Deerfield Beach, Fla.)* **2010**, *22*, 361.
[46] J. N. Grima, K. E. Evans, *J. Mater. Sci. Lett.* **2000**, *19*, 1563.
[47] Y. Cho, J.-H. Shin, A. Costa, T. A. Kim, V. Kunin, J. Li, S. Y. Lee, S. Yang, H. N. Han, I.-S. Choi, D. J. Srolovitz, *Proc. Natl. Acad. Sci.* **2014**, *111*, 17390.
[48] T. Mullin, S. Deschanel, K. Bertoldi, M. C. Boyce, *Phys. Rev. Lett.* **2007**, *99*, 084301.
[49] D. Garcia-Gonzalez, M. Hossain, *Extreme Mech. Lett.* **2021**, *48*, 101382.
[50] M. Rambausek, D. Mukherjee, K. Danas, *Comput. Meth. Appl. Mech. Eng.* **2022**, *391*, 114500.
[51] M. A. Moreno-Mateos, K. Danas, D. Garcia-Gonzalez, *Mech. Mater.* **2023**, *184*, 104742.